

Temperature Bounds on X-ray jets in the solar atmosphere

G.T. Farrell, King's College

Abstract

Coronal X-ray jets are small phenomena found in coronal holes, distinguished by an outward collimated plasma flow and brightening at the base of the flow. Such jets could have some impact in two questions in heliophysics, the first being that of what powers the solar wind, and the second being that of the coronal heating problem. While many properties of jets have been thoroughly studied with large sample sets, the temperature of these jets is less well known. This project looks at data taken from the Atmospheric Imaging Assembly aboard the Solar Dynamics Observatory for four jet events, three 'blowout' jets and one 'standard' jet, and uses regularised differential emission measure inversion to analyse their temperatures. It was found that jets have strong emissions in the 0.8-3MK range, with blowout jets also exhibiting emissions at around 10MK.

1 Introduction

Extreme ultraviolet (EUV) jets in the quiet Sun were first discovered in 1983 (Brueckner and Bartoe 1983), and the first proper observations of these were made in the 1990s by Shibata et al. who used the Soft X-Ray Telescope (SXT) aboard the Yohkoh satellite (Shibata et al. 1992). These phenomena are characterised by collimated plasma flow moving outwards from the solar corona, with a bright spot at the foot forming an ‘inverted-Y’ shape (Moore, Sterling, et al. 2013; Moreno-Insertis and Galsgaard 2013; Shibata et al. 1992) as in figure 1.

Moore, Cirtain, et al. (2010) proposed a binary classification of jets: ‘standard’ jets and ‘blowout’ jets, which differ in their morphologies and temperature features (Pucci et al. 2013), as well as some aspects of their mechanism (Moore, Sterling, et al. 2013; Moreno-Insertis and Galsgaard 2013). Standard jets, as seen in figure 1, have a single, ‘simple’ spire and a bright spot at the foot, whereas blowout jets have a more complex, multi-strand spire with a bright arch as well as a bright spot (Moore, Sterling, et al. 2013). Blowout jets are thought to be hotter (Pucci et al. 2013), but also always exhibit a ‘cool’ He II 304Å emission ($\sim 5 \times 10^4$ K) (Moore, Sterling, et al. 2013).

Shibata et al. (1992) proposed a mechanism for standard jets, illustrated in figure 2, in which a low density region of plasma – which creates the magnetic arch at the base of the jet – emerges into the corona and into the ambient, unipolar field. The opposite polarity of the arch and the ambient field creates a current sheet between the ambient field and the opposite-polarity leg of the arch. As the ‘plasma mountain’ continues to emerge into the corona, the current sheet becomes large enough and thin enough to cause reconnection across it. This reconnection process releases the magnetic free energy previously trapped in the current sheet, which is converted to thermal energy via Joule heating (Moreno-Insertis and Galsgaard 2013). This forms two fields: the open field, which forms the spire of the jet, and the closed field which forms the bright point at the foot in the opposite-polarity region. These reconnected lines carry plasma out away from the corona in the case of the open field, and back into the corona in the case of the closed field.

Further work expanding on the mechanism behind jets (and, notably, applying to blowout jets as well) was done by Moreno-Insertis and Galsgaard (2013) using a numerical simulation of flux rope emergence into the ambient field, and its violent ejection.

Two statistical surveys of jets, done by Sako, Shimojo, and Kitabayashi (2012) and Savcheva et al. (2007) give some indication of the basic properties of jets, the results of which are transcribed in table 1.

Some other studies of the physical parameters of jets have been carried out (Culhane et al. 2007; Doschek et al. 2010; Madjarska 2011; Nisticò et al. 2011; Pucci et al. 2013; Shimojo

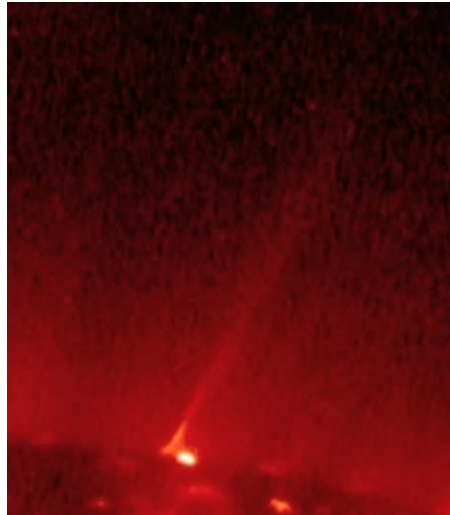


Figure 1: An image of a standard jet taken by the Hinode X-ray telescope on 10/01/2007 at 18:50. The bright spot is clearly visible at the foot of the jet, slightly off-centre, forming one arm of the ‘inverted-Y’. The spire of the jet is slightly less clear, but visible pointing towards the top-right of the image.

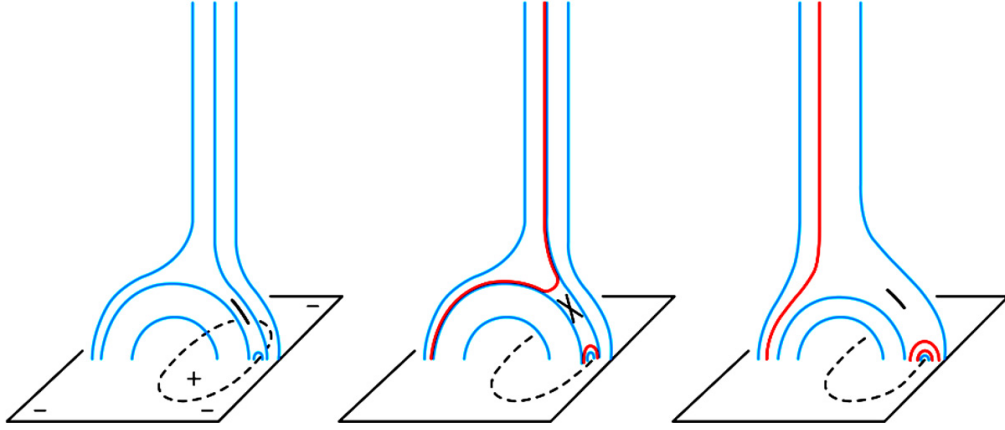


Figure 2: The standard jet mechanism proposed by Shibata et al. (1992), courtesy of Moore, Sterling, et al. (2013). The left-most image shows the emergence of the ‘plasma mountain’ of opposite polarity into the ambient field, and the formation of the current sheet. The middle image shows the burst of reconnection across the current sheet, tearing it down. The right-most image shows the newly reconnected open field line (left) and closed field line (right).

	Savcheva et al. (2007)	Sako, Shimojo, and Kitabayashi (2012)
frequency (day^{-1})	60	50
lifetime (minutes)	~ 10	~ 10
height (10^4 km)	5	2.9
base width (10^3 km)	8	4.4
outward velocity (km/s)	160	180

Table 1: Some physical properties of jets.

Study	Instruments	Spatial Res.	Cadence	Analysis Method	Result
Shimojo and Shibata (2000)	SXT	2.5''/px	30s	Filter ratio	3-8MK
Culhane et al. (2007)	EIS, XRT	1-2.1''/px	1-3m	Lightcurves	2-3MK
Doschek et al. (2010)	EIS	2.1''/px	3m	DEM iteration	1.4MK
Madjarska (2011)	SUMER, EUVI	1.6''/px	2.5-10m	Filter ratio	12MK
Nisticò et al. (2011)	EUVI, COR	1.6''/px	2.5-10m	Isothermal DEM	0.8-1.3MK
Pucci et al. (2013)	XRT, EUVI	1-1.6''/px	1-10m	Isothermal DEM	1.5MK

Table 2: Previous studies of jet temperatures using a variety of instruments and methods. EUVI is the EUV Imager aboard the STEREO satellites; COR is the Coronagraph, also aboard STEREO; XRT is the Hinode X-Ray Telescope; SXT is the Soft X-Ray Telescope on Yohkoh; EIS is the EUV Imaging Spectroscoper on Hinode; SUMER is the Solar Ultraviolet Measurements of Emitted Radiation project which is aboard SOHO, the Solar and Heliospheric Observatory. The analysis methods are explained in the Methodology section.

and Shibata 2000), all of which also look at the temperature of the jets, and these results are summarised in table 2.

The presence of EUV jets in the solar corona has two possible, interesting effects. The first is that, since the open field line carries a lot of plasma outwards from the corona, the jets could be at least partly responsible for powering the solar wind (Brueckner and Bartoe 1983; Moore, Sterling, et al. 2013). The second possible effect is the heating of the solar corona, since a portion of the plasma heated by the reconnection event is confined by the closed field in the corona. This latter effect could provide part of the solution to the coronal heating problem (Moore, Sterling, et al. 2013). Put simply, the coronal heating problem is to identify the processes that heat the solar corona to millions of degrees Kelvin, whereas the photosphere sits at around 6000 K. Why the corona is several hundred times hotter than the photosphere is not known, although magnetic reconnection has been put forward as a possible explanation (Klimchuk 2006; Moore, Sterling, et al. 2013).

The results published by Sako, Shimojo, and Kitabayashi (2012) and Savcheva et al. (2007) are quite well established, as the sample sizes used were large. Here we aim to get good bounds on the temperatures of x-ray jets. Previous studies of the temperature bounds on jets have not used instruments of as good a spatial resolution and cadence as those that this project uses, and have used methods with larger uncertainties than this project, as can be seen in table 2; this is explained in more detail in the next section.

2 Methodology

Data for this project come from two sources: the Hinode satellite – a JAXA-NASA-ESA joint mission launched in 2006 – and the Solar Dynamics Observatory – launched in 2010 by NASA as part of the Living With a Star (LWS) programme. On board the Hinode satellite is the X-Ray Telescope (XRT), which has a resolution of 1 arcsecond / pixel and a cadence of 1 minute (*XRT Fact Sheet* n.d.). The XRT has a number of filters, with quite broad response functions as in figure 3.

On board the SDO is the Atmospheric Imaging Assembly (AIA) which has a higher resolution of 0.6 arcseconds / pixel and a cadence of 10 seconds (in practice the maximum cadence of frames it is possible to request is 12 seconds) (*AIA Instrument Specification* n.d.). The AIA

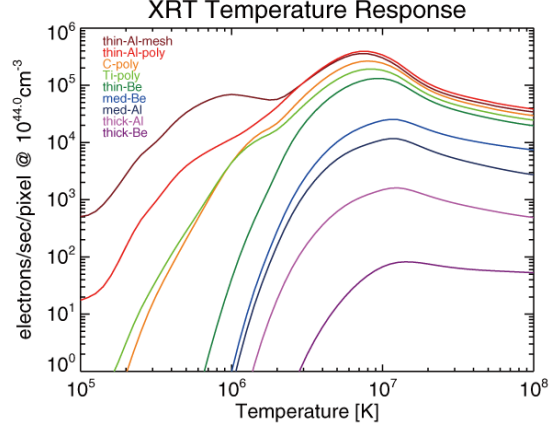


Figure 3: XRT Filter Response Functions from *XRT Fact Sheet* (n.d.).

has seven EUV channels, six of which cover high temperatures as in figure 4. These channels have peaks in the response functions that are much narrower than those of the XRT. This means that temperature estimates from AIA data are more accurate than those from XRT data, because the peaks are more distinct in the different channels.

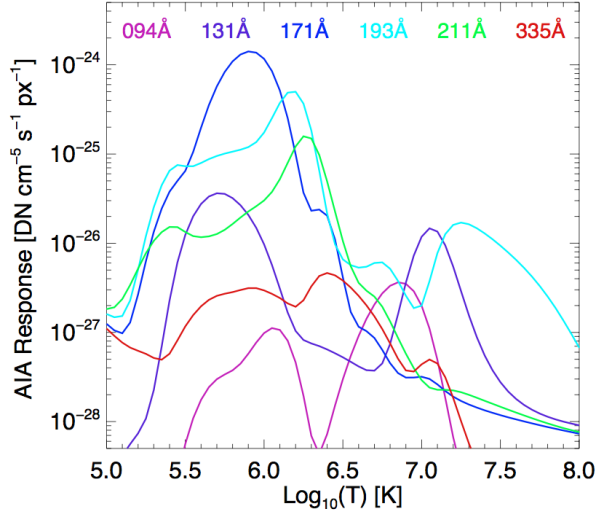


Figure 4: AIA Filter Response Functions from Hannah and Kontar (2012).

The XRT follows Hinode Operation Plans (HOPs), which are specified field-of-view and filter combinations designed to study a particular phenomenon. As such, XRT does not observe the full solar disc continually in all its channels. The AIA, on the other hand, provides continual observation of the full solar disc, making it easier to select exactly which data are required for study. The more narrow field of view of the XRT, however, is ideal for the initial search for jets. HOPs were selected for which the XRT was focussed on a coronal hole, and

then the Hinode ‘QuickLook’ videos¹ were examined to find suitable jets to study. A list of jets drawn up by Sterling and Moore (as yet unpublished) was also used to help narrow down the search. This list covered forty-four events, from July 2010 to April 2011 and from that a short-list was created of sixteen jets. This was further reduced to four events, listed in table 4, that would be used for further investigation.

The process of selecting events was on the basis of two criteria: events had to be after the launch of the SDO in 2010, and the jets had to be ‘clear’. Jets are most visible on the limb of the Sun, because the ejection trajectory is mostly in the plane of the sky, and thus perpendicular to the line of sight. These events, however, are also set against coronal radiation from other parts of the limb, which sits between the observer and the event jet, and also in the background of the image. This reduces the clarity with which we can observe a particular jet. An example of this problem can be seen in Nisticò et al. (2011). While limb events are useful for measuring the physical dimensions of the jets, this study is only looking at the emissions and so the background and foreground radiation is more problematic. Thus jets closer to the centre of the solar disc were used. All of the selected jets were also in coronal holes, meaning that there was very little extra radiation interfering with the data.

The improved resolution and cadence of the AIA as compared to the XRT made it better for studying the jets in detail. Once the jet events had been selected, data was downloaded from the Lockheed Martin AIA Cutout Service². This allowed a restricted field of view to be selected and AIA frames downloaded for a given time period. The reason for using the cutout service is that, while ‘level 1’ data (full disc) could be downloaded directly from various SDO archives, these frames are very large, so downloading an entire time series of them was slow and unnecessary (and prone to failure). The cutout service provided a simple way of selecting these frames, but was not without its problems, which will be detailed in due course.

In order to process and analyse the AIA data, a library of custom procedures and functions was written by the author in the Interactive Data Language (IDL)³, making use of some of the functions in the SolarSoftWare (SSW) libraries⁴. This custom library was designed specifically to work with jets, but can easily be applied to work with any type of study that uses AIA data to analyse the temperature emissions of an event. The library is governed by an Open Source license, and has been published on GitHub⁵. A programme listing can be found in the appendices of this report.

The tools created for this project used frames from the cutout service for two purposes, the first was to create videos of the events. This made it possible to see the evolution of the morphological features of the events in different filters. The second was to produce lightcurves – normalised filter intensity plotted against time – of the events. The normalisation process involved dividing the data numbers by the exposure time, since different filters had different exposure times in each frame, in order to get commensurable intensities. As was seen in figure 4, each filter has a response function relating to a temperature scale. This is due to the fact that filters are not pure, and respond to several different wavelengths, which, in turn, correspond to a range of ions in the atomic spectra (O’Dwyer et al. 2010). An example of this for two of the AIA channels can be seen in figure 5. The AIA response curves used in this project were calculated using version 7 of the CHIANTI atomic database (Dere et al. 1997;

¹http://hinode.nao.ac.jp/QLmovies/index_e.shtml

²http://www.lmsal.com/get_aia_data/

³<http://www.exelisvis.com/ProductsServices/IDL.aspx>

⁴<http://www.lmsal.com/solarsoft/>

⁵<https://github.com/gfarrell/solar-jets-analysis>

Landi, Del Zanna, et al. 2012). The filters used in the AIA have some characteristic features, as can be seen in table 3 and are discussed in O’Dwyer et al. (2010). Thus, by plotting the filters against time, one can get a rough idea of the temperature features of an event and how they evolve.

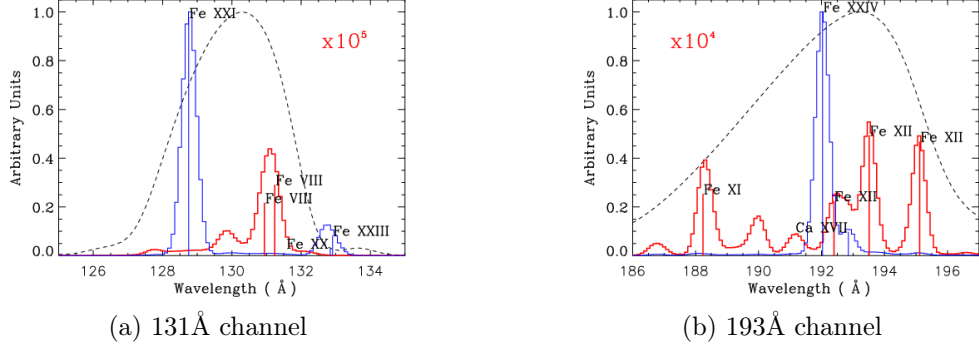


Figure 5: Spectral responses of two AIA channels, courtesy of O’Dwyer et al. (2010). Synthetic spectra for flares are in blue, and for the quiet sun in red. The dashed line is the effective area of the filter.

Channel	Primary ions	Characteristic T /MK
94Å	Fe X, XVIII	1, 6
131Å	Fe VIII, XX, XXIII	0.4, 10, 16
171Å	Fe IX	0.6
193Å	Fe XII, XXIV	1.3, 20
211Å	Fe XIV	2
304Å	He II	0.05
335Å	Fe XVI	2.5

Table 3: Table of filters and their approximate characteristic temperatures along with the primary ions that they correspond to. These give an idea of what the filter responds to. Reproduced from *AIA Instrument Specification* (n.d.).

In order to estimate the temperature of coronal emissions, regularised differential emission measure (DEM) inversion was used. The observed intensity of an optically thin spectral line emitted from a transition from upper level j to lower level i , with wavelength λ_{ij} in a volume V is:

$$I(\lambda_{ij}) = \frac{h\nu_{ij}}{4\pi} \int_V N_j(X^{+m}) A_{ji} dV \text{ [ergs s}^{-1} \text{ sr}^{-1}] \quad (1)$$

Where the transition from j to i occurs spontaneously with probability A_{ji} , releasing photons of frequency ν_{ij} . The number density of the upper level (j) of the ion is $N_j(X^{+m})$. The volume of plasma is normally defined by the spatial resolution of the instrument: $V = Sh$, where S is the projected area of the instrument’s aperture, and h is the line of sight through the emitted plasma. With some basic assumptions about the processes that populate and de-populate atomic excitement levels, the intensity of the line can be re-written as an integral along the line of sight (Del Zanna and Mason 2013):

$$I(\lambda_{ij}) = \int_h N_e N_H A(X) G(N_e, T, \lambda_{ij}) dh \quad (2)$$

Here, $A(X)$ is the abundance of element X with respect to Hydrogen, and $G(N_e, T, \lambda_{ij})$ (frequently just $G(T)$) is the “contribution function”, which is calculated from atomic data taken from CHIANTI (Dere et al. 1997; Landi, Del Zanna, et al. 2012).

The DEM, denoted by $\xi(T)$, characterises the emission for a given temperature, T , and can be defined if there is a unique relationship between N_e and T .

$$\xi(T) = N_e N_H \frac{dh}{dT} [\text{cm}^{-5} \text{ K}^{-1}] \quad (3)$$

$$\int_T \xi(T) dT = \int_h N_e N_H dh \quad (4)$$

That is, $\xi(T)$ indicates the amount of plasma emitting in the interval $[T, T + dT]$ along the line of sight. Thus, for a spectral line (if we assume $A(X)$ to be constant along the line of sight):

$$I(\lambda_{ij}) = A(X) \int_T G(T) \xi(T) dT \quad (5)$$

Note that in (5) $G(T)$ is still actually $G(N_e, T, \lambda_{ij})$, but is written as a function of temperature because of the strong temperature dependence, not to mention that we have stipulated a unique relationship between N_e and T . Filters such as those used in the AIA, however, respond to a number of spectral lines, as can be seen in figure 5, and hence the observed intensity in a given filter, I_i is a result of the convolution of the response function for that filter, $R_i(T)$, and the DEM (Hannah and Kontar 2012; O’Dwyer et al. 2010).

$$I_i = \int_T R_i(T) \xi(T) dT \quad (6)$$

I_i is observed and R_i is calculated from the CHIANTI data, and are thus “known” quantities. (6) gives us a set of Fredholm integrals of the first kind (one for each channel), and inversion of this is not straightforward (Del Zanna and Mason 2013), so $\xi(T)$ cannot be inferred from multi-wavelength data (Hannah and Kontar 2012). Constraints have to be introduced in order to reconstruct the DEM. The simplest approach (used by Madjarska (2011), Nisticò et al. (2011), Pucci et al. (2013), and Shimojo and Shibata (2000)) is to assume that the plasma is isothermal (i.e. $\xi(T) = \delta(T - T_0)$), which means that the ratio of emissions for two filters is equal to the ratio of the filter response functions at T_0 . As Hannah and Kontar; Nisticò et al. note, the isothermal assumption is erroneous, and therefore introduces uncertainties. A more accurate method – regularised inversion – is explained in Hannah and Kontar (2012) and used in this project. This method introduces additional constraints for ‘smoothness’ of the DEM, which reduces the amplification of uncertainties as different possible DEM curves are iterated over, improving on other DEM iteration methods such as that used by Doschek et al. (2010). An IDL implementation of this algorithm, provided by Dr. Hannah⁶, was used in this project.

The lightcurves were used to select time slices of the events to analyse for the temperature using DEM inversion. Initially, this was attempted using the same data from the cutout service

⁶<http://www.astro.gla.ac.uk/~iain/demreg/map/>

that were used to generate the lightcurves and videos. As was mentioned, however, using the cutout service is not without problems. In order for the DEM library to process the AIA data, it has to be concatenated into a single array, one map⁷ for each filter. When the cutout service created the image files, at least one filter tended to have slightly different dimensions to the others (normally by one pixel). In IDL, in order for structures to be included together in an array, they must be identical, so this difference in the image sizes prevented the data from being included in a single array, and thus from being processed. In order to circumvent this problem, part of the library created for this project is able to select, download and process ‘AIA level 1’ data directly from the Virtual Solar Observatory (VSO), an archive of SDO data. That all the processing is done by the library itself prevents any such issues arising.

Jet events are relatively small and faint phenomena, meaning that the data counts in the AIA data are quite low, which increases the uncertainty in the DEM. To work around this, the original images were resampled by a factor of two. This halved the resolution of the image, but increased the certainty of the resulting DEM. Before resampling, the low counts of the AIA data meant that the signal-to-noise ratio (SNR) tolerance of the DEM inversion algorithm had to be relaxed from a default of $\text{SNR} > 3$ to $\text{SNR} > 1$. This increased the uncertainty in the DEM emissions. Having resampled the data by a factor of two, thus increasing the counts, the SNR requirement was re-tightened to $\text{SNR} > 3$, which, as can be seen in figure 6, reduced the size of the horizontal error bars – a measure of the uncertainty in the DEM.

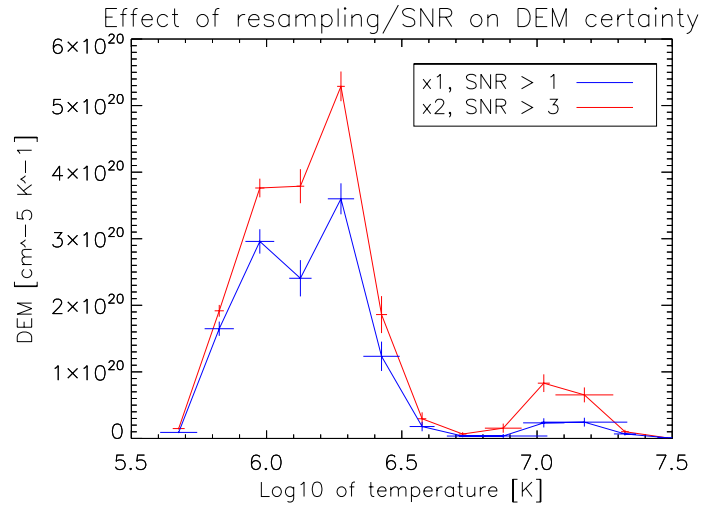


Figure 6: A comparison of the effect of resampling and the SNR constraint on DEM certainty. The un-resampled graph (blue) has a more relaxed SNR constraint ($\text{SNR} > 1$), because of the lower counts. The $\times 2$ resampled graph (red) increases the data counts in each pixel, allowing a tighter SNR constraint. This reduces the horizontal error bars, which are an indication of the certainty of the DEM.

⁷A ‘map’ in this context is an IDL data structure which contains a 2×2 array of image data, along with various metadata such as the filter name, exposure time, position, units &c.. More information can be found at *IDL Map Software for Analyzing Solar Images* (n.d.).

The library used Iain Hannah’s algorithm to process the resampled images, with the $\text{SNR} > 3$ restriction, and temperature bins in the range $5.6 \leq \log_{10}(T) \leq 7.55$ with a 0.15 interval in \log_{10} space. Initially this was set to $5.6 \leq \log_{10}(T) \leq 7.2$, to cover the range of expected temperatures, but the upper bound was increased to $\log_{10}(T) = 7.55$ when it became obvious that most of the jets were exhibiting emissions around the 10MK mark. Since temperature is a continuous quantity, the algorithm operates by calculating the emissions for a particular temperature bin. The bin size used here was $\log_{10}(T_2) - \log_{10}(T_1) = 0.15$. Intuitively, it seems that increasing the number of bins (and hence decreasing the bin size) would increase the resolution of the graph (at the cost of more processing time), suggesting that the interval used in this project is arbitrarily high. In fact, given that DEM inversion is an ill-constrained problem (Hannah and Kontar 2012), increasing the number of bins beyond a certain point only serves to amplify the uncertainties, which results in the uncertainty in any particular bin causing it to overlap with its neighbours, so no information is gained. An illustration of this can be seen in figure 7.

Unfortunately, despite the resampling of the original AIA data, there are still many pixels in the DEM emissions that are missing data because the counts are low, and so the SNR tolerance constraint isn’t satisfied in those pixels (as can be seen in figure 8). To circumvent this issue, instead of plotting the emission graph for a particular (spatial) point on an event, an average of the emissions was taken across a small area (thus also avoiding the problem of temperature variations across a feature). This average emission was then plotted instead of the emission for a particular point. The $\text{SNR} > 3$ constraint exacerbates this problem, with the result that only the bright spot has high enough counts to get any temperature readings at all. Therefore, in order to study the fainter phenomena (like the spire, and the background corona), the constraint was relaxed.

While events were selected for their clarity to reduce background and foreground emissions from interfering with those of the jets, an uncertain level of background coronal radiation would still have been present in the data. In order to examine the temperature contributions of the jet, data were downloaded for each event at a point in time before the jet erupted (but not so far in advance that the coronal conditions might have significantly changed). This was then plotted with the jet emissions such that a comparison could be made, and the true contributions of the jets themselves could be identified.

In the introduction, it was stated that this project uses more accurate instruments and more certain methods than previous studies. As can be seen in table 2, the AIA has a better spatial resolution and cadence than the instruments of previous studies. It can also be seen that the most common method used in previous studies was a filter ratio method. Taking Nisticò et al. (2011) as an example, the authors used an imaging device to reconstruct an emission measure. This was done taking two channels: 171Å and 195Å, and comparing the response curves in order to get a single-valued function as in figure 9. Using only two filters gives access to less information than the six that are used in this project, and hence the emission measure is less certain, but as Nisticò et al. (2011) note, it also requires the assumption that the plasma is isothermal, which, as was noted above, is inaccurate. This introduces additional uncertainty. The use of regularised DEM inversion in this project avoids this problem and also allows the use of six channels, providing more information than with previous studies which used the filter ratio method.

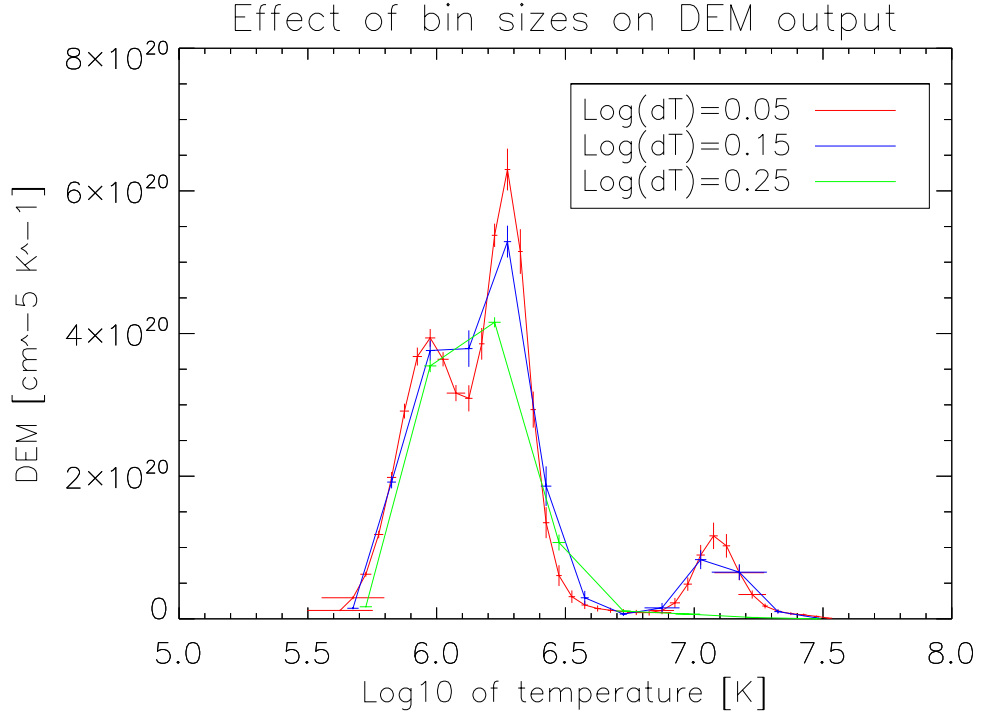


Figure 7: A comparison of DEM graphs calculated using different bin sizes. Here dT is the interval between two temperatures, since the bin sizes are measured in \log_{10} space. All three graphs are quite different (although they resemble each-other). The graph with the highest resolution (red) has horizontal errors which overlap with other points, and so we have not really gained information. On the other hand, the graph with the lowest resolution (green) lacks detail. The graph with a bin size of 0.15 in \log_{10} space (blue) strikes a good balance between overlapping error bars and lack of detail.

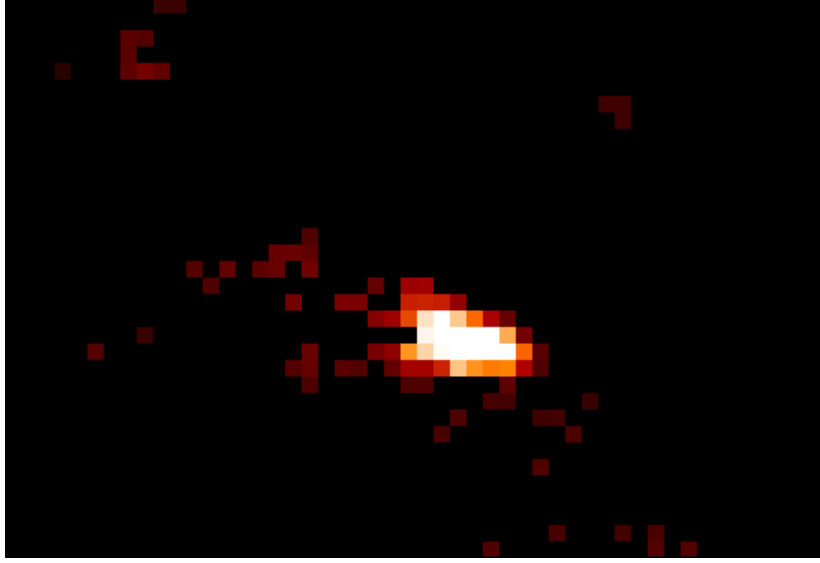


Figure 8: Example aggregate of DEM emissions for a jet. Many pixels are black, indicating that there was insufficient data to reconstruct the DEM there at the specified SNR tolerance.

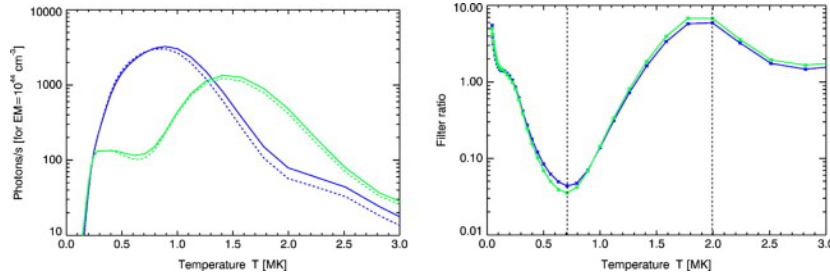


Figure 9: Filter ratio method from Nisticò et al. (2011). On the left are the response functions for the EUVI A and B channels, and on the right is the ratio of the two response functions. Notice that the range of this function has to be restricted such as to make it continuous but also single-valued.

3 Results

As has been mentioned in the previous section, four jet events were selected for study in this project (table 4), snapshots of which can be seen in figure 10, taken mid-way through the jets' evolution. The morphological features of the jets are illustrated in figure 11.

#	Date	Time	Lifetime /mins	X /arcsecs	Y /arcsecs	size /(arcsecs \times arcsecs)
1	2010-08-26	11:15	~ 12	-115	880	$\sim 20 \times 10$
2	2010-08-28	13:34	~ 26	-65	835	$\sim 30 \times 12$
3	2010-09-05	21:18	~ 16	40	850	$\sim 25 \times 20$
4	2010-09-05	01:11	~ 7	-45	915	$\sim 8 \times 25$

Table 4: Table of jet events studied in this project. Sizes and lifetimes are approximate and only for illustration.

Figure 12 shows the lightcurves for each jet, taken over the whole jet, and all show an obvious peak in most of the channels during the jets' eruption. From the existence of a 'cool' 304Å component (purple) in figures 12a, 12b and 12c, it would seem that jets 1-3 are blowout jets (Moore, Sterling, et al. 2013), whereas in figure 12d, the 304Å channel does not exhibit a peak during the jet eruption outside of the noise level in that channel (i.e. the 304Å channel has an $\text{SNR} \lesssim 1$), suggesting that it is a standard jet (Moore, Sterling, et al. 2013). The 193Å and 171Å channels have the strongest peaks, probably responding to 0.6-1.3MK (table 3). There is also quite a strong response in the 211Å channel, which is likely to be indicative of a 2MK component in the emissions. This is weaker in jet 4 than in jets 1-3.

As can be seen from figure 13, all the jets show strong temperature components in the range $5.9 \leq \log_{10}(T) \leq 6.5$, i.e. $0.8\text{MK} \lesssim T \lesssim 3\text{MK}$. Additionally, jets 1-3 exhibit a small contribution from $7 \leq \log_{10}(T) \leq 7.3$ ($10\text{MK} \lesssim T \lesssim 20\text{MK}$). As has been mentioned, jets 1-3 are likely to be blowout jets, whereas jet 4 is probably a standard jet, as evidenced by figure 12. Blowout jets release more energy during reconnection than standard jets (Pucci et al. 2013), which explains the lack of high temperature (10-20MK) components in jet 4 compared to jets 1-3.

From looking at figure 13 it is clear that the high temperature components are concentrated in the bright spot. This is unsurprising since, as explained in the introduction, the bright spot is formed of a closed reconnected field line, whereas the spire is formed of an open field line. Thus the spire expands as it moves away from the foot of the jet, cooling as it does so, whereas the bright spot is confined and therefore does not cool (and possibly even heats up) as the jet evolves. It is interesting to look at how the temperature of the bright spots compares across these jets, since it is the plasma in the bright spot that is being fed back into the solar corona (possibly heating it).

As is seen in figure 15, jets 1 and 2 are similar, and jets 3 and 4 are similar. As explained previously, jet 4 does not exhibit the same strength of high temperature features, and is also the only jet lacking a 10-20MK component. That jet 3 is similar to jet 4 could be as a result of the fact that it is the smallest and faintest event, as can be seen in figure 11. This means that much of the captured DEM emissions will be of the background corona, which will make it look like the cooler components (0.8-1MK) are relatively stronger. Nevertheless, it still exhibits strong peaks in the high temperature components, and, notably, the 10-20MK region.

It is true of all the jet events that the background coronal emission will contribute to

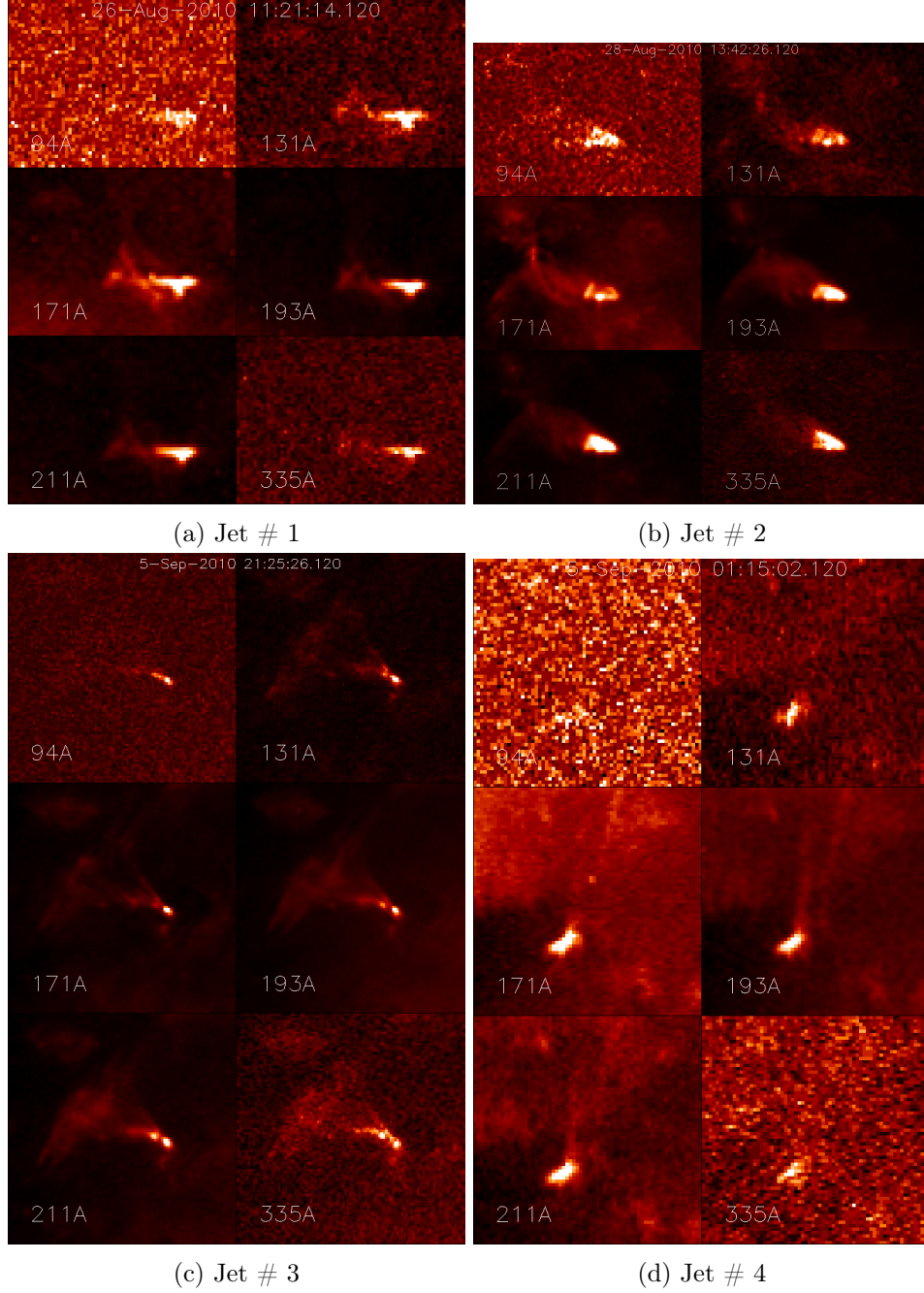
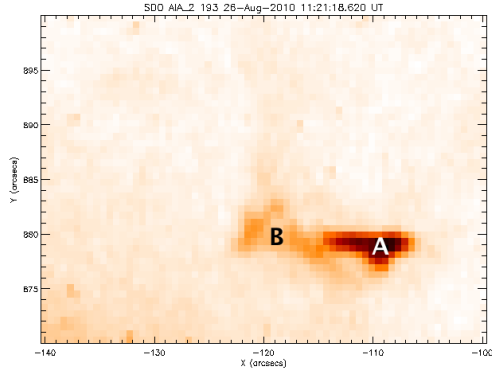
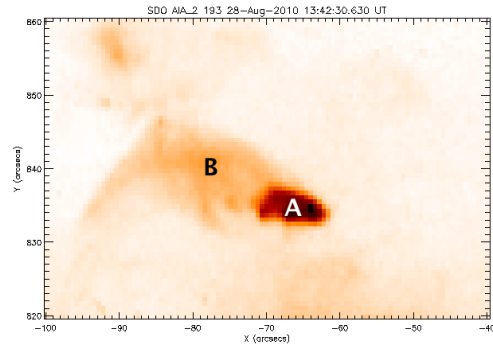


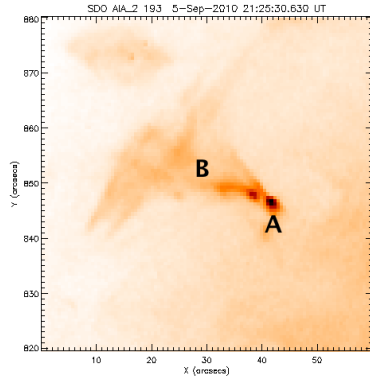
Figure 10: Images of the four jet events in each of the AIA channels examined. Reading the rows from left to right and top to bottom, the channels are 94Å, 131Å, 171Å, 193Å, 211Å, 335Å.



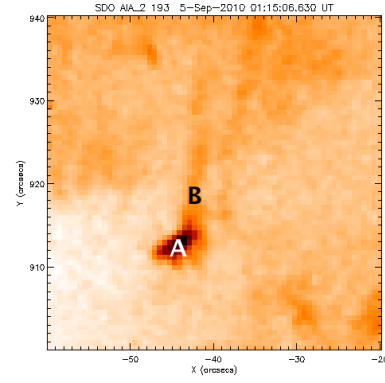
(a) Jet # 1



(b) Jet # 2

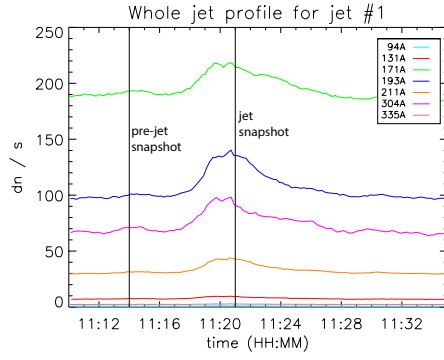


(c) Jet # 3

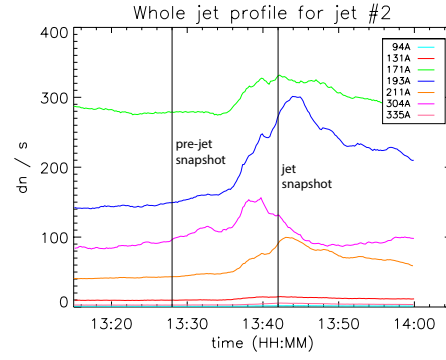


(d) Jet # 4

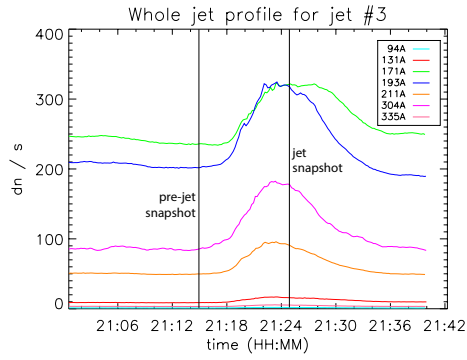
Figure 11: Images of the four jet events in the 193Å channel taken from the VSO with the bright spot and spire labelled with “A” and “B”, respectively. The jets tend to be clearest in this channel, so it was used for illustration purposes. Additionally, the colours have been inverted for clarity.



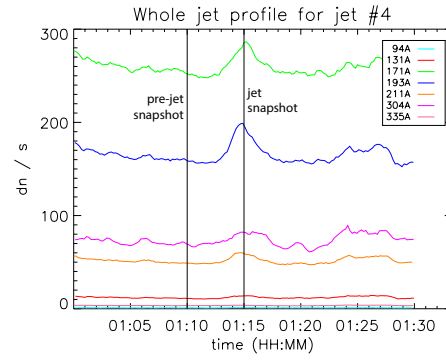
(a) Jet # 1



(b) Jet # 2

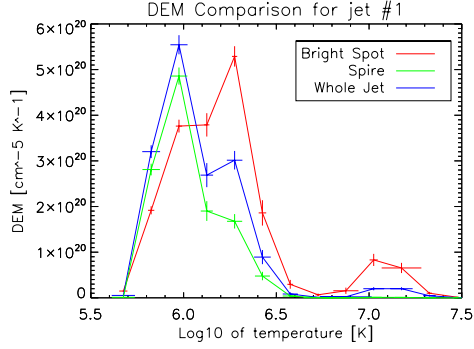


(c) Jet # 3

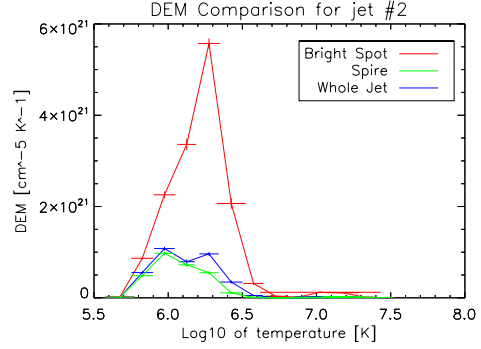


(d) Jet # 4

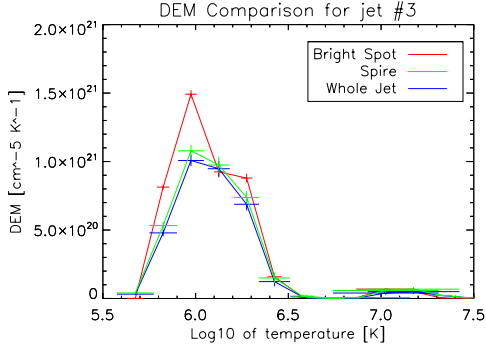
Figure 12: Intensity profiles for each jet, averaged over the whole jet (see figure 14), the horizontal lines mark where snapshots were taken for DEM analysis.



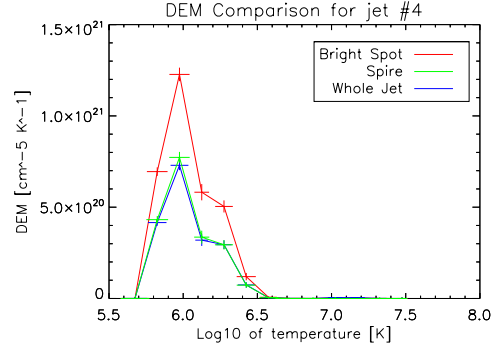
(a) Jet # 1



(b) Jet # 2

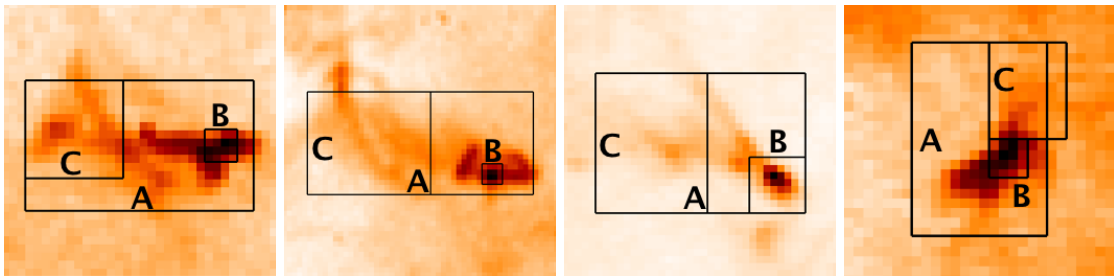


(c) Jet # 3



(d) Jet # 4

Figure 13: DEM emissions for each jet in three areas: the bright spot, the spire and the whole jet. The reason that the counts are mostly much higher in the bright spot than for the whole jet, is that the areas were averaged over. Since the bright spot is quite well defined in the images, it fit well into the bounding rectangles (see figure 14), whereas the whole jet did not fit well into a rectangle, and thus many ‘dark’ pixels were included in the average, reducing the counts.



(a) Jet # 1

(b) Jet # 2

(c) Jet # 3

(d) Jet # 4

Figure 14: Rectangular boxes indicate the areas over which the DEM was averaged for the whole jet (A), bright spot (B) and spire (C). Colours have been inverted for clarity.

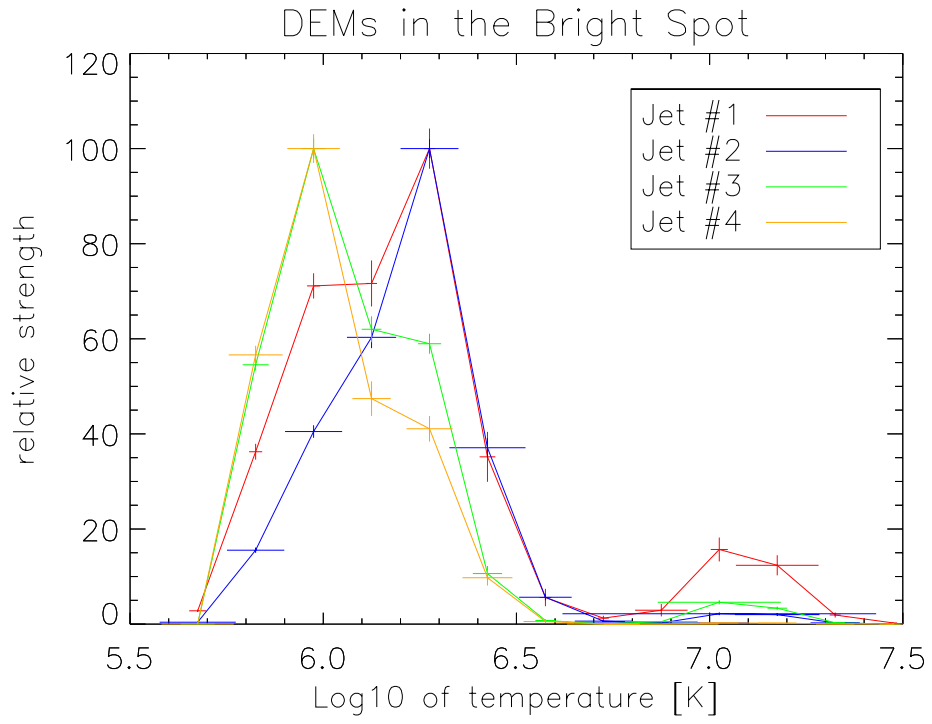
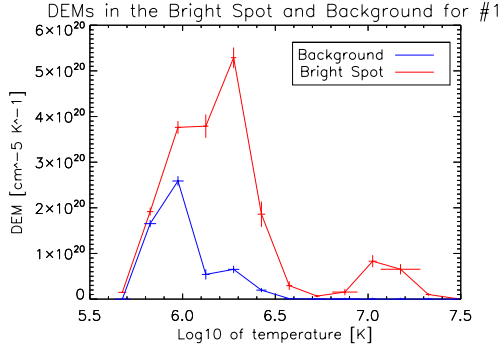
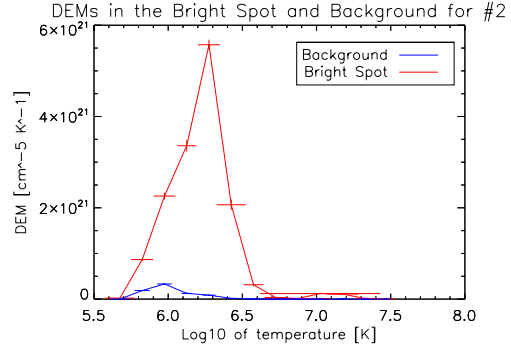


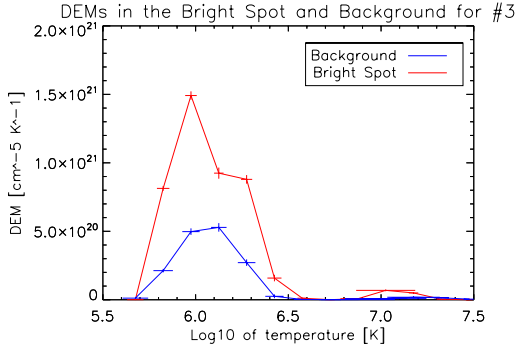
Figure 15: Comparison of the DEM emissions for the bright spots of each jet. The peaks are ‘relative’ in the sense that, in order to make them commensurable, the counts (y-axis) are as a percentage of the maximum count.



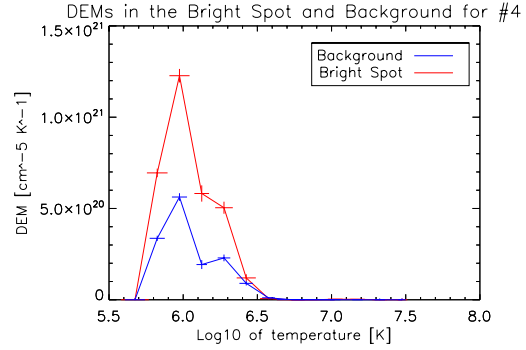
(a) Jet # 1



(b) Jet # 2



(c) Jet # 3

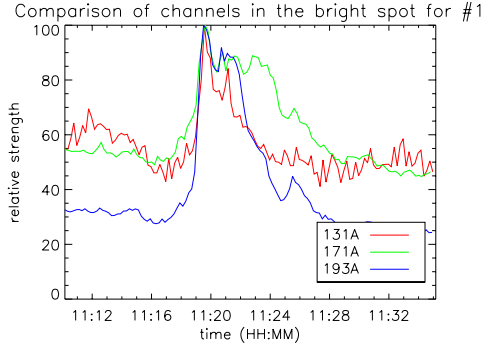


(d) Jet # 4

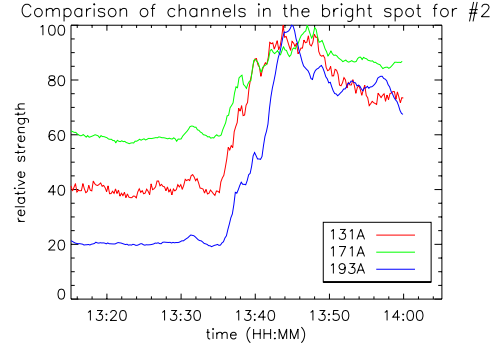
Figure 16: Comparison of the background coronal emission (blue) to that of the bright spot (red).

the DEM, even though it was minimised by choosing events in coronal holes. Therefore it is interesting to see how the bright spot emissions compare to the coronal background. For reference, figure 12 shows whence these ‘snapshots’ of the jets and coronal background were taken in terms of the jet evolution. From figure 16, it is clear that, for the most part, the corona tends to contribute most to the lower temperature components (around $\log_{10}(T) \sim 6.0$), and there is no 10-20MK contribution from the corona (as one would expect). The difference is most marked in jets 1 and 2, where it is clear that the 2-3MK and 10-20MK components are almost completely contributed by the jet itself. This suggests that the jets have temperature emissions in the 2-3MK range and the 10-20MK range for blowout jets, with almost no emissions in the range 4-8MK.

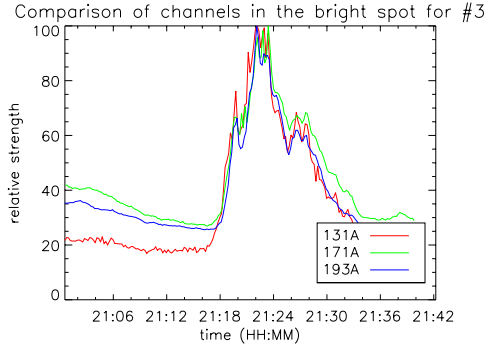
The combination of the 10-20MK components being unexpectedly high given previous studies of jets (table 2) and that there are almost no emissions in the range 4-8MK raises the question as to whether the 10-20MK contribution is real. Given the ill-constrained nature of the DEM, it is conceivable that this would be an artefact of the algorithm and this was initially thought.



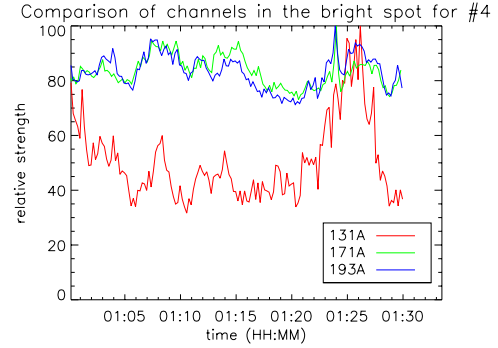
(a) Jet # 1



(b) Jet # 2



(c) Jet # 3



(d) Jet # 4

Figure 17: A comparison of the 131Å, 171Å and 193Å channels in the bright spots of each jet. The intensities have been normalised, in that they are scaled to a percentage of the maximum intensity to make them easily comparable.

From table 3, the 131Å and 171Å channels are one ionisation band apart (Fe VIII and Fe XX vs. Fe IX). The former has characteristic temperatures around 0.4MK and 10MK, whereas the latter has temperatures around 0.6MK, which is the lower end of the coronal temperature scale. If these two channels had similar intensity profiles as a function of time in figure 12 then we could suppose that they are responding to similar temperature regions. It is clear in figure 17, that the 131Å and 171Å channels deviate from each other (this most visible for jets 1 and 2), and the 131Å intensity falls off more quickly than the 171Å. This difference could be suggestive of the 131Å channel responding to a higher temperature component in jets 1-3. The idea that the 131Å channel is indeed responding to high temperature components in jets 1-3 is supported by the lack of any strong signal in that channel for jet 4, since it also lacks a high temperature component in figure 13d.

Furthermore, in looking at figure 13, the horizontal error in the $\log_{10}(T) = 7.05$ peak is comparable to that of the other major temperature features. Conversely, the $\log_{10}(T) = 7.2$ peak, which corresponds to around 16MK, has a large horizontal error in all the jets, suggesting

that the uncertainty is high enough in this component that we can discount it being a ‘real peak’. This does support the hypothesis that the 10MK component is actually present in the blowout jets, which was unexpected, given that jets are quite small and faint compared to hotter phenomena like flares.

4 Conclusions

From studying image data in different EUV channels from the AIA, and analysing these data by DEM inversion and by using lightcurves, it appears that both standard and blowout jets are characterised by strong temperature emissions in the 2-3MK region. There are also emissions from 0.8-2MK, but these are also strong in the coronal background as can be seen in figure 16. This fits into the aggregate range of temperatures from previous studies (being hotter than some, and cooler than others) as seen in table 2, but the instruments used in this project were more accurate, and the methods less uncertain. It was also found that blowout jets have emissions at around 10MK, which is higher than most of the previous studies (with the exception of Madjarska (2011)) but compares well with the model in Moreno-Insertis and Galsgaard (2013), which suggests that through Joule heating the temperatures could rise to the order of 10^7 K. This could add some support to models that suggest that blowout jets release more energy in the reconnection event than standard jets (Pucci et al. 2013). Although emissions as high as 20MK were exhibited, it seems unlikely that these reflect the actual emissions from the Sun.

As to the coronal heating problem, while the results here give bounds on the temperature of EUV jets in the corona, they are still very small and faint phenomena, albeit quite frequent. While it is unlikely that jets contribute significantly to the heating of the corona because of the small fraction of the sun that they cover, further theoretical and experimental work will be necessary to ascertain the degree to which they contribute to local heating.

The results should also prove useful in improving the models of jet evolution, like that proposed by Moreno-Insertis and Galsgaard (2013), by providing more accurate temperature parameters for the different morphological features of the events.

5 Improvements and further research

While the methods and instruments used here have been more accurate than previous studies, there is room for improvement. The uncertainty in the 20MK emissions could be resolved by introducing a wider range of data covering other wavelengths. From figure 3, it is clear that the XRT ‘thick’ filters have broad response functions in the high temperature region, but do not respond to lower temperatures. Including data from these filters could help determine the validity of the DEM at higher temperatures. These data were not included here because, as was mentioned in the introduction, XRT data are not available for all channels at all times. Time constraints also made it impractical to include these data for this project.

The DEM inversion algorithm and library provided by Hannah and Kontar (2012) was developed initially to look at flares, and has been shown to work well with such events. This is the first time it has been used to look at jets, which are much fainter and smaller events. It is possible that some tweaking of the algorithm and its parameters would improve the certainty of the DEM. The library also used AIA filter data generated using version 7 of the CHIANTI atomic database (Dere et al. 1997; Landi, Del Zanna, et al. 2012). New atomic data are now

available (Landi, Young, et al. 2013), and this should be factored into any further work as the new data will improve the accuracy of the DEM.

While the AIA has a good spatial resolution for viewing jets, as has been explained the data counts were still quite low, introducing uncertainties into the results. New, more accurate and more sensitive instruments such as NASA’s Interface Region Imaging Spectrograph (IRIS) mission⁸ and the joint NASA-ESA Solar Orbiter mission⁹ (when launched in 2017) could provide additional data to help resolve these uncertainties.

Finally, the above results are for a small sample size of only four jet events. The tools created during this project should make it easier, in the future, to more quickly analyse a much larger sample set, which will give greater insight into jets, especially into the differences between the standard and blowout types.

6 Acknowledgements

This project owes much to the guidance of Dr. Helen Mason and Dr. Giulio Del Zanna. The DEM analysis would have been considerably more difficult, and less accurate, without the library of Dr. Iain Hannah (and his support when problems were encountered). The list of events created by Dr. Alfonse Sterling and Dr. Ronald Moore was extremely helpful in the search for suitable jets for analysis.

Hinode is a Japanese mission developed and launched by ISAS/JAXA, collaborating with NAOJ as domestic partner, and NASA (USA) and STFC (UK) as international partners. Scientific operation of the Hinode mission is conducted by the Hinode science team organized at ISAS/JAXA. This team mainly consists of scientists from institutes in the partner countries. Support for the post-launch operation is provided by JAXA and NAOJ, STFC, NASA, ESA (European Space Agency), and NSC (Norway).

The Solar Dynamics Observatory was developed and launched by NASA (USA) as part of the Living with a Star (LWS) programme. The Atmospheric Imaging Assembly was developed by the Lockheed Martin Solar and Astrophysics Laboratory (LMSAL). LMSAL also provided the data cutout service, which played a vital rôle in the initial data procurement. The Virtual Solar Observatory is a joint NASA-Stanford (USA) project to archive solar data, and was used to obtain data on the jets for analysis.

CHIANTI is a collaborative project involving George Mason University, the University of Michigan (USA) and the University of Cambridge (UK).

I am extremely grateful to both the Hinode and SDO teams for their efforts in designing, building and operating these missions, as well as the team behind the VSO for maintaining such an archive.

⁸http://www.nasa.gov/mission_pages/iris

⁹<http://science.nasa.gov/missions/solar-orbiter/>

References

- AIA Instrument Specification*. URL: <http://aia.lmsal.com/public/instrument.htm>.
- Brueckner, G. E. and J.-D. F. Bartoe (1983). “Observations of high-energy jets in the corona above the quiet sun, the heating of the corona, and the acceleration of the solar wind”. In: *The Astrophysical Journal* 272, pp. 329–348. DOI: 10.1086/161297.
- Culhane, L. et al. (2007). “Hinode EUV Study of Jets in the Sun’s South Polar Corona”. In: *Publications of the Astronomical Society of Japan* 59, p. 751. DOI: 10.1093/pasj/59.sp3.S751.
- Del Zanna, G. and H. Mason (2013). “The Sun as a Star”. In: *Planets, Stars and Stellar Systems. Volume 4: Stellar Structure and Evolution*. Ed. by T. D. Oswalt and M. A. Barstow, p. 87. DOI: 10.1007/978-94-007-5615-1_3.
- Dere, K. P. et al. (1997). “CHIANTI - an atomic database for emission lines”. In: *Astronomy and Astrophysics Supplement series* 125, pp. 149–173. DOI: 10.1051/aas:1997368.
- Doschek, G. A. et al. (2010). “Bright Points and Jets in Polar Coronal Holes Observed by the Extreme-Ultraviolet Imaging Spectrometer on Hinode”. In: *The Astrophysical Journal* 710, pp. 1806–1824. DOI: 10.1088/0004-637X/710/2/1806.
- Hannah, I. G. and E. P. Kontar (2012). “Differential emission measures from the regularized inversion of Hinode and SDO data”. In: *Astronomy and Astrophysics* 539, A146, A146. DOI: 10.1051/0004-6361/201117576. arXiv: 1201.2642 [astro-ph.SR].
- IDL Map Software for Analyzing Solar Images*. URL: http://hesperia.gsfc.nasa.gov/rhessidatcenter/complementary_data/maps/.
- Klimchuk, J. A. (2006). “On Solving the Coronal Heating Problem”. In: *Solar Physics* 234, pp. 41–77. DOI: 10.1007/s11207-006-0055-z. eprint: astro-ph/0511841.
- Landi, E., G. Del Zanna, et al. (2012). “CHIANTI - An Atomic Database for Emission Lines. XII. Version 7 of the Database”. In: *The Astrophysical Journal* 744, 99, p. 99. DOI: 10.1088/0004-637X/744/2/99.
- Landi, E., P. R. Young, et al. (2013). “CHIANTI - An Atomic Database for Emission Lines. XIII. Soft X-Ray Improvements and Other Changes”. In: *The Astrophysical Journal* 763, 86, p. 86. DOI: 10.1088/0004-637X/763/2/86.
- Madjarska, M. S. (2011). “Dynamics and plasma properties of an X-ray jet from SUMER, EIS, XRT, and EUVI A & B simultaneous observations”. In: *Astronomy and Astrophysics* 526, A19, A19. DOI: 10.1051/0004-6361/201015269. arXiv: 1008.3983 [astro-ph.SR].

- Moore, R. L., J. W. Cirtain, et al. (2010). “Dichotomy of Solar Coronal Jets: Standard Jets and Blowout Jets”. In: *The Astrophysical Journal* 720.1, p. 757. URL: <http://stacks.iop.org/0004-637X/720/i=1/a=757>.
- Moore, R. L., A. C. Sterling, et al. (2013). “The Cool Component and the Dichotomy, Lateral Expansion, and Axial Rotation of Solar X-Ray Jets”. In: *The Astrophysical Journal* 769, 134, p. 134. DOI: 10.1088/0004-637X/769/2/134.
- Moreno-Insertis, F. and K. Galsgaard (2013). “Plasma Jets and Eruptions in Solar Coronal Holes: A Three-dimensional Flux Emergence Experiment”. In: *The Astrophysical Journal* 771, 20, p. 20. DOI: 10.1088/0004-637X/771/1/20. arXiv: 1305.2201 [astro-ph.SR].
- Nisticò, G. et al. (2011). “Determination of temperature maps of EUV coronal hole jets”. In: *Advances in Space Research* 48, pp. 1490–1498. DOI: 10.1016/j.asr.2011.07.003.
- O’Dwyer, B. et al. (2010). “SDO/AIA response to coronal hole, quiet Sun, active region, and flare plasma”. In: *Astronomy and Astrophysics* 521, A21, A21. DOI: 10.1051/0004-6361/201014872.
- Pucci, Stefano et al. (2013). “Physical Parameters of Standard and Blowout Jets”. In: *The Astrophysical Journal* 776.1, p. 16. URL: <http://stacks.iop.org/0004-637X/776/i=1/a=16>.
- Sako, N., M. Shimojo, and T. Kitabayashi (2012). “Statistical Study of X-ray Jets in the Polar Region”. In: *Hinode-3: The 3rd Hinode Science Meeting*. Ed. by T. Sekii, T. Watanabe, and T. Sakurai. Vol. 454. Astronomical Society of the Pacific Conference Series, p. 153.
- Savcheva, A. et al. (2007). “A Study of Polar Jet Parameters Based on Hinode XRT Observations”. In: *Publications of the ASJ* 59, p. 771.
- Shibata, K. et al. (1992). “Observations of X-ray jets with the YOHKOH Soft X-ray Telescope”. In: *Publications of the ASJ* 44, pp. L173–L179.
- Shimojo, M. and K. Shibata (2000). “Physical Parameters of Solar X-Ray Jets”. In: *The Astrophysical Journal* 542, pp. 1100–1108. DOI: 10.1086/317024.
- XRT Fact Sheet*. URL: http://hinode.nao.ac.jp/xrt_e/fact_sheet_e.shtml.

A Solar Jets Library

The library written by the author for this project is available at <https://github.com/gfarrell/solar-jets-analysis> and contains the following programmes. Full documentation for this library will be made available at the above address, and the source code is commented.

A.1 Data procurement and preparation

1. **compile_maps** compiles maps into an ordered array of channels.
2. **sdo_get_snapshot** downloads “snapshot” image files for a given date and time from the VSO.
3. **sdo_process_full** processes cutout data from the LMSAL cutout service and prepares them for analysis.
4. **sdo_process_snapshot** processes “snapshot” data once downloaded and prepares them for analysis.

A.2 DEM processing

1. **attenuate_dem** normalises DEM data to a percentage of the maximum value.
2. **dem_diff** calculates the difference between two sets of DEM data.
3. **dem_sum** sums a series of emission measures for different temperatures.
4. **generate_dem** takes AIA level 1 data and generates DEMs from them.

A.3 Graph plotting

1. **aia_plot_resp** plots AIA response functions given a data file.
2. **compare_dems** averages DEMs over a specified area and plot the results against each other.
3. **lightcurve** takes AIA time series data and generates normalised intensity plots against time.

A.4 Image and video creation

1. **data2gif** takes AIA data and turns them into a GIF video.
2. **data2movie** creates an IDL movie from AIA data.
3. **images_layout** lays out a series of images in rows and columns.
4. **plot_areas_on_snapshot** plots rectangular boxes on snapshot images to indicate areas.
5. **plot_frames** plots frames (as images) from AIA cutout data (time series).

6. **plot_snapshot** plots the 193Å channel from a snapshot as an image.
7. **stitch_frames** takes AIA data and stitches frames from a channel's time series to contemporaneous frames in other channels, creating a video of all the channels at once.
8. **view_snapshot** displays and labels channels from a snapshot in a single image.
9. **visualise_dem** plots DEM emissions as an image for given temperature(s).

A.5 Utility programmes

1. **choosefile** allows the interactive or programmatic choosing of files.
2. **configurator** configures the environment with various paths.
3. **copy_window** clones a window.
4. **demload** loads DEM data for an event.
5. **dload** loads AIA data for an event.
6. **findoptimaldecomposition** decomposes a number into two factors that are closest to the square root.
7. **prompt** various user input functions.
8. **promptchoice** allows users to choose between given options.
9. **save_window** saves the pixels of a window to a specified PNG file.
10. **sigfigs** rounds a number to a specified number of significant figures.